

Article

Photocatalytic Activities of g-C₃N₄ (CN) Treated with Nitric Acid Vapor for the Degradation of Pollutants in Wastewater

Ruishuo Li ¹, Bingquan Wang ² and Rui Wang ^{1,*} ¹ School of Environmental Science and Engineering, Shandong University, Qingdao 266237, China² School of Chemistry and Molecular Engineering, Qingdao University of Science and Technology, Qingdao 266042, China

* Correspondence: wangrui@sdu.edu.cn

Abstract: In this article, we reported a novel setup treatment using nitric acid vapor to treat g-C₃N₄ (CN). By treatment with nitric acid vapour, the basic structure of the CN has not been destroyed. These adoptive treatments enhanced the photocatalytic performance of CN and were reflected in the elimination of rhodamine B (RhB) as well as tetracycline hydrochloride (TC). In comparison to CN, CN-6 demonstrated the highest photocatalytic yield for the breakdown of RhB (99%, in 20 min). Moreover, the excellent reuse of CN-6 for breaking down RhB was also demonstrated. This clearly demonstrated that treatment with nitric acid vapor promoted a blue shift, positively extended its valence band position, and increased the oxidizability of the holes. This also caused CN to disperse better into the aqueous phase, introducing more oxygen-containing functional groups. Thus, treatment with nitric acid vapor has the potential to be applied to delaminate the CN in order to enhance photocatalytic activity.

Keywords: g-C₃N₄; photocatalytic activity; rhodamine B; tetracycline hydrochloride; degradation; wastewater



Citation: Li, R.; Wang, B.; Wang, R. Photocatalytic Activities of g-C₃N₄ (CN) Treated with Nitric Acid Vapor for the Degradation of Pollutants in Wastewater. *Materials* **2023**, *16*, 2177. <https://doi.org/10.3390/ma16062177>

Academic Editor: Raphaël Schneider

Received: 26 December 2022

Revised: 21 February 2023

Accepted: 2 March 2023

Published: 8 March 2023



Copyright: © 2023 by the authors. Licensee MDPI, Basel, Switzerland. This article is an open access article distributed under the terms and conditions of the Creative Commons Attribution (CC BY) license (<https://creativecommons.org/licenses/by/4.0/>).

1. Introduction

Due to industrialization and population growth, many countries have critical environmental issues, such as energy crises and pollution of the environment [1]. Nowadays, the development of state-of-the-art technologies to address these issues at a global scale is of great importance [2,3]. Among various proposed technologies, photocatalytic technology has tremendously gained global attention to alleviate environmental contamination because of its ability to make direct use of inexhaustible solar power [4–6]. Although one of the earliest investigated photocatalysts is titanium dioxide (TiO₂), it exhibits significant limitations due to the large band gap and responds only to ultraviolet light [7,8]. As a visible light active photocatalyst, metal-free graphitic carbon nitride (g-C₃N₄) has recently attracted a lot of attention. It has distinctive properties for photocatalysis, such as a tunable band gap (2.7 eV), single optical properties to harvest sunlight, high stability to resist photo-corrosion, suitable electronic properties, environmental friendliness, and low cost [9–13]. Though the g-C₃N₄ exhibited immense potential in the photocatalysis field, it still suffers from poor active sites, a low redox potential of photogenerated charge carriers, a low quantum yield, and a poor dispersion of the aqueous phase [14,15].

Several modifications have been developed to ameliorate the photocatalytic performance of the bulk g-C₃N₄, such as element doping [16–18], heterojunction building [19,20], and morphology controlling [21,22]. Motivated by the pioneering work on graphene [23], many researchers have made efforts to delaminate the bulk g-C₃N₄ into 2D thinner counterparts and explore their novel properties. The ultrathin 2D g-C₃N₄ nanosheet has distinct physicochemical properties that set it apart from bulk g-C₃N₄, such as a broader bandgap, a higher redox ability of charge carriers, an open-up surface, and an extended life for charge

carriers. These properties give g-C₃N₄ nanosheets improved photocatalytic performance in real-world applications [24–26].

Niu and his coworkers first developed g-C₃N₄ nanosheets by long-time thermal oxidation exfoliation that increased bandgap and ameliorated the capacity of electron transport. The super photocatalytic activities of g-C₃N₄ nanosheets as photocatalysts were established via H₂ evolution [27]. Yan et al. successfully exfoliated g-C₃N₄ in hot water to obtain ultrathin g-C₃N₄. The as-prepared g-C₃N₄ ultrathin has a thickness of 1.2 nm after 12 h of treatments, with a wide lateral dimension and improved photoactivity for the degradation of organic dye when exposed to visible light [28]. Miao et al. synthesized 2D g-C₃N₄ nanosheets with acid treatment that demonstrated an excellent photocurrent response close to 0.5 mA/cm² and lower charge transfer resistance [29]. Although the majority of the currently used techniques (such as thermal exfoliation, liquid etching, and chemical exfoliation using potent oxidizing acids) can exfoliate bulk g-C₃N₄ into a single layer, they are also ineffective because the tri-s-triazine units are destroyed, the processing time is prolonged, and the yield of nanosheets is subpar [30]. Therefore, it is advisable to develop an advanced strategy with high efficiency and low energy consumption for delaminating bulk g-C₃N₄ to ultrathin g-C₃N₄ nanosheets.

Herein, we present a simple process to prepare g-C₃N₄ nanosheets through nitric acid vapor treatment using a new practical carbon material processor invented by our research group. Compared with aqueous exfoliation, the process has the merits of a controllable treatment time, avoiding over-oxidation, easy collection of products, and high yield. The obtained nanosheets were studied according to the crystal structure, surface group, composition, and physicochemical properties. The g-C₃N₄ nanosheets were found to exhibit a stronger oxidizing capacity and disperse well into an aqueous solution. As anticipated, when exposed to visible light, g-C₃N₄ nanosheets demonstrated outstanding photocatalytic activity and stability for the destruction of RhB and TC. Moreover, a proper mechanism and the active species for the degradation of RhB were also studied through scavenger experiments.

2. Materials and Methods

2.1. Materials

Urea was bought from Bodi (Tianjin, China). Tetracycline hydrochloride (TC) was obtained from Shanghai Ruiyong Biotechnology Co., Ltd (Shanghai, China). Triethanolamine (TEOA), concentrated nitric acid and absolute ethanol were purchased from Fuyu (Tianjin, China). Rhodamine B (RhB) was purchased from Kemiou (Tianjin, China). p-Benzoquinone (p-BQ) was purchased from Shanghai Macklin Biochemical Co. Ltd (Shanghai, China). All reagents were of analytical grade and used with no further purification.

2.2. Synthesis of the Photocatalysts

The bulk g-C₃N₄ was prepared using the method reported previously [31]. In a nutshell, 20.0 g of urea was placed in a 100 mL crucible with a cover slip and heated in a muffle furnace to 550 °C for 3 h at a rate of 17.8 °C/min. After being allowed to cool to ambient temperature, the resulting yellow substance was ground into a powder in an agate mortar. The synthesized sample was denoted as CN.

The alteration to the bulk g-C₃N₄ was treated with nitric acid vapor. Some concentrated HNO₃ was poured into a flask with three necks, and g-C₃N₄ was added to the processing apparatus as shown in Figure 1. The self-assembling device was then placed in a 170 °C oil bath for a period of time. According to the treatment time, the g-C₃N₄ was named CN-X (X = 2, 4, 6, 8 h).

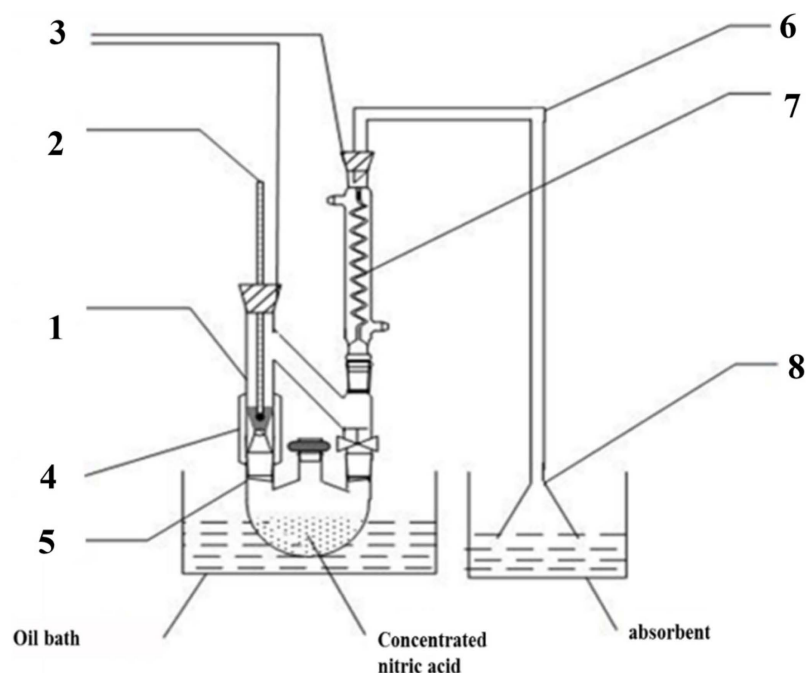


Figure 1. Self-made HNO₃ vapor treatment device ((1): steam treatment device, (2): thermometer, (3): rubber plug, (4): heating belt, (5): three-mouth flask, (6): catheter, (7): snake condensation tube, (8): funnel).

2.3. Characterization

X-ray diffraction (XRD) patterns were obtained by a Bruker D8 ADVANCE instrument using Cu-K α radiation ($\lambda = 0.15405$ nm, 40 KV \times 60 mA) from 10° to 80° (2 θ) with a scanning rate of 0.02°/s. X-ray photoelectron spectroscopy (XPS) was obtained by a Thermo ESCALAB 250XI with a monochromated Al K α X-ray source. A Bruker ALPHA-T Fourier transform infrared spectrometer was used to record the Fourier transform infrared spectra (FT-IR) of the samples, with a range from 400 to 4000 cm⁻¹ using the KBr pellet at room temperature. Brunauer–Emmett–Teller (BET) measurement was used to determine the specific surface area of samples (Quantachrome Instruments Quadrasorb SI, United States Quantachrome Co., Ltd, Boulder, CO, USA). Using a 100 kV accelerating voltage, a field emission scanning electron microscope (SEM) (JSM-6700) was used to characterize the morphologies of the samples. A UV-vis spectrophotometer was used to generate diffuse reflectance spectra (DRS) (SHIMADZU, UV-2550). Photoluminescence (PL) spectroscopy was performed at room temperature using a Hitachi F-4500 fluorescence spectrophotometer.

2.4. Photocatalytic Performance Tests

2.4.1. Photocatalytic Experiments

Under visible light irradiation, TC and RhB were used as target pollutants to evaluate the photocatalytic activities of the as-prepared samples. For photocatalytic experiments, a photocatalytic reactor with a 200 mL beaker as a reaction vessel and a 300W-Xenon lamp with a 420 nm cutoff filter as a visible light source was used, with constant concurrent magnetic stirring. Typically, 25 mg photocatalysts were introduced into 100 mL RhB solution (10mg/L) and 50 mg photocatalysts were introduced into 100 mL TC solution (20 mg/ L). The mixture was then sonicated for 5 min and magnetically stirred in the dark for 30 min to achieve an equilibrium between adsorption and desorption. After a specific time interval of irradiation, 4 mL of the suspension was removed and filtered through a 0.22 μ m filter membrane to remove the photocatalyst. A UV-vis spectrophotometer was used to measure the concentrations of TC and RhB. (SP-756PC, Shanghai Spectrum Instruments Co., Ltd, Shanghai, China).

2.4.2. Determination of Active Species during Photocatalytic Degradation

Radical trapping experiments were performed to ensure the presence of active species in the RhB photo-degradation process. In this study, p-Benzoquinone (p-BQ), triethanolamine (TEOA), and isopropanol (IPA) were used as scavengers of holes (h^+), hydroxyl radicals ($\bullet OH$), and superoxide radicals ($\bullet O_2^-$), respectively. Prior to reaching the adsorption equilibrium, the capture agents were added to the RhB solution (10 mg/L) and agitated for 30 min without light. The photocatalytic reaction experiment was then performed.

3. Results and Discussion

3.1. Characterization of the As-Prepared Photocatalysts

3.1.1. Structure and Morphology Characterizations

Figure 2 displays the XRD patterns of the samples to examine the impact of HNO_3 vapor on the crystalline phase of $g-C_3N_4$. The two distinct peaks at 12.97° and 27.59° for all samples were the in-plane (100) diffraction reflecting the interlayer stacking of the $g-C_3N_4$ aromatic units and the interlayer (002) diffraction reflecting the structural packing pattern of the aromatic segments in the plane, respectively [32]. Nitric acid steam treatment improved the interlayer stacking interaction of the aromatic conjugated system by gradually increasing the (002) peak intensity of $g-C_3N_4$ in comparison to untreated $g-C_3N_4$. This shows that nitric acid steam treatment can break the hydrogen bond between $g-C_3N_4$ layers and cause the $g-C_3N_4$ layers to peel off into nanostructures [33]. Henceforth, this confirms that the crystalline phase of $g-C_3N_4$ is unaffected following treatment with nitric acid vapor. Fourier transform infrared (FT-IR) spectra were used to study the structural information of pure and processed $g-C_3N_4$. Figure 3 demonstrates that the C-N heterocycles' stretching vibrations at $1200\text{--}1650\text{ cm}^{-1}$ and the triazine units' distinctive breathing vibration at 810 cm^{-1} were present in all the samples, indicating that the tri-s-triazine units' chemical core structure is resistant to HNO_3 vapor erosion. However, as the bulk of $g-C_3N_4$ was exfoliated, both the N-H and O-H stretching vibrations steadily increased, indicating that the increased density of the $-OH$ group in $g-C_3N_4$ was caused by the acid hydrolysis action of the bridging N groups [34].

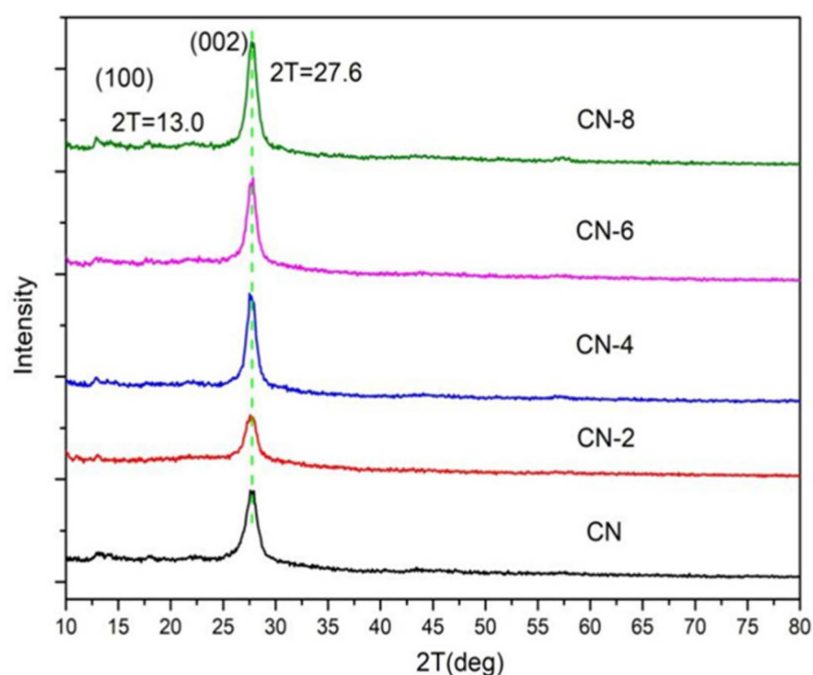


Figure 2. XRD patterns of the samples.

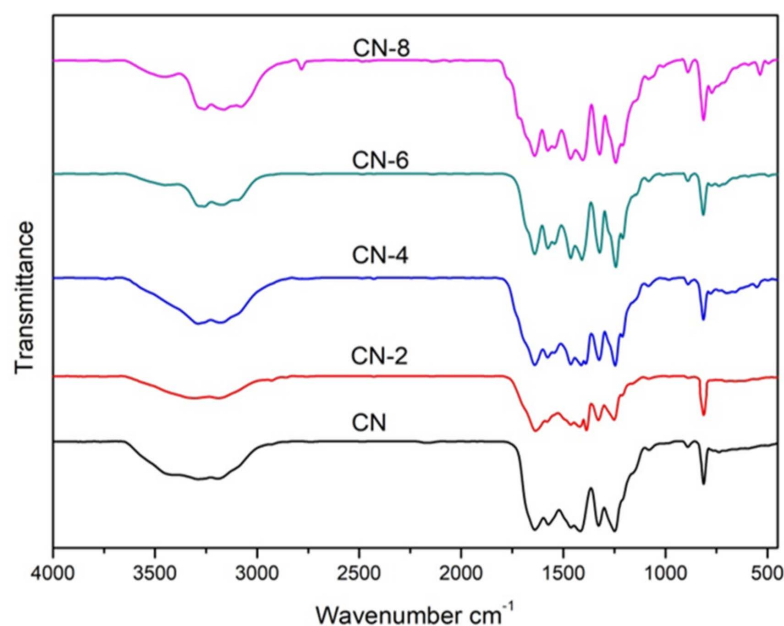


Figure 3. FT-IR spectra of samples.

X-ray photoelectron spectroscopy (XPS) was used to determine the elemental surface composition and chemical state of $g\text{-C}_3\text{N}_4$ (Figure 4). The XPS spectrum in Figure 4a indicates that all the samples are mainly composed of C, N, and O. Figure 4b shows the high-resolution XPS spectrum of C 1s for the bulk $g\text{-C}_3\text{N}_4$ and treated $g\text{-C}_3\text{N}_4$, in which the four peaks at 284.6 eV, 286.0 eV, 288.1 eV and 289.4 eV can be attributed to C = C, C-NH₂, N-C = N, and C-O [35]. When CN-6 was compared to bulk $g\text{-C}_3\text{N}_4$, the intensity of the peak at 286.0 eV and 289.4 eV was increased. This could be attributed to C-O groups formed during the acid hydrolysis of the tri-s-triazine unit, which bridged C-N-C [36]. The intensity of the peak at 286.0 eV and 289.4 eV increased when CN-6 was compared to bulk $g\text{-C}_3\text{N}_4$. C-O groups formed during the acid hydrolysis of the tri-s-triazine unit, which bridged C-N-C, could be responsible for this. Figure 4c displays the XPS spectra for O 1s of the bulk $g\text{-C}_3\text{N}_4$ and CN-6 catalysts. The asymmetrical O 1s spectra of the two samples could be deconvoluted into these components at 533.5 eV, 532.1 eV, and 530.8 eV, attributable to the chemisorbed water, surface-adsorbed oxygen species, and surface lattice oxygen, respectively. Interestingly, the N 1s high-resolution spectrum (Figure 4d) revealed three typical peaks at 398.8 eV, 400.1 eV, and 404.4 eV corresponding to the C-N = C, -NH₂, and graphitic species, respectively [37]. The XPS results show the stability of $g\text{-C}_3\text{N}_4$ preserved even after nitric acid vapor treatment.

The surface characteristics of samples from the N₂ adsorption–desorption isotherms (Figure 5) were similar. A type-IV isotherm with a hysteresis loop was obtained in both the pure and treated $g\text{-C}_3\text{N}_4$, indicating the presence of mesoporous structures. CN-6's BET surface areas decreased by 25.7 m²/g when compared to bulk $g\text{-C}_3\text{N}_4$ (105.6 m²/g), and its pore volume decreased by 0.278 ccg⁻¹. This is attributed to the bulk $g\text{-C}_3\text{N}_4$ being exfoliated to nanosheets, then the partially completed nanosheets begin to aggregate and stack [38]. Meanwhile, the original macropore was destroyed [33]. The morphology of pure and treated $g\text{-C}_3\text{N}_4$ can be illustrated via SEM images shown in Figure 6. From Figure 6a, we can see that $g\text{-C}_3\text{N}_4$ samples with rough structures were composed of flake-like, aggregated, and different micron-sizes stacking layers, which are consistent with the typical characteristics of $g\text{-C}_3\text{N}_4$ prepared through the method of polymerization [39,40]. In Figure 6b, bulk $g\text{-C}_3\text{N}_4$ was exfoliated into nanosheets and morphologically changed to cubic and spherical shapes after nitric acid vapor treatment.

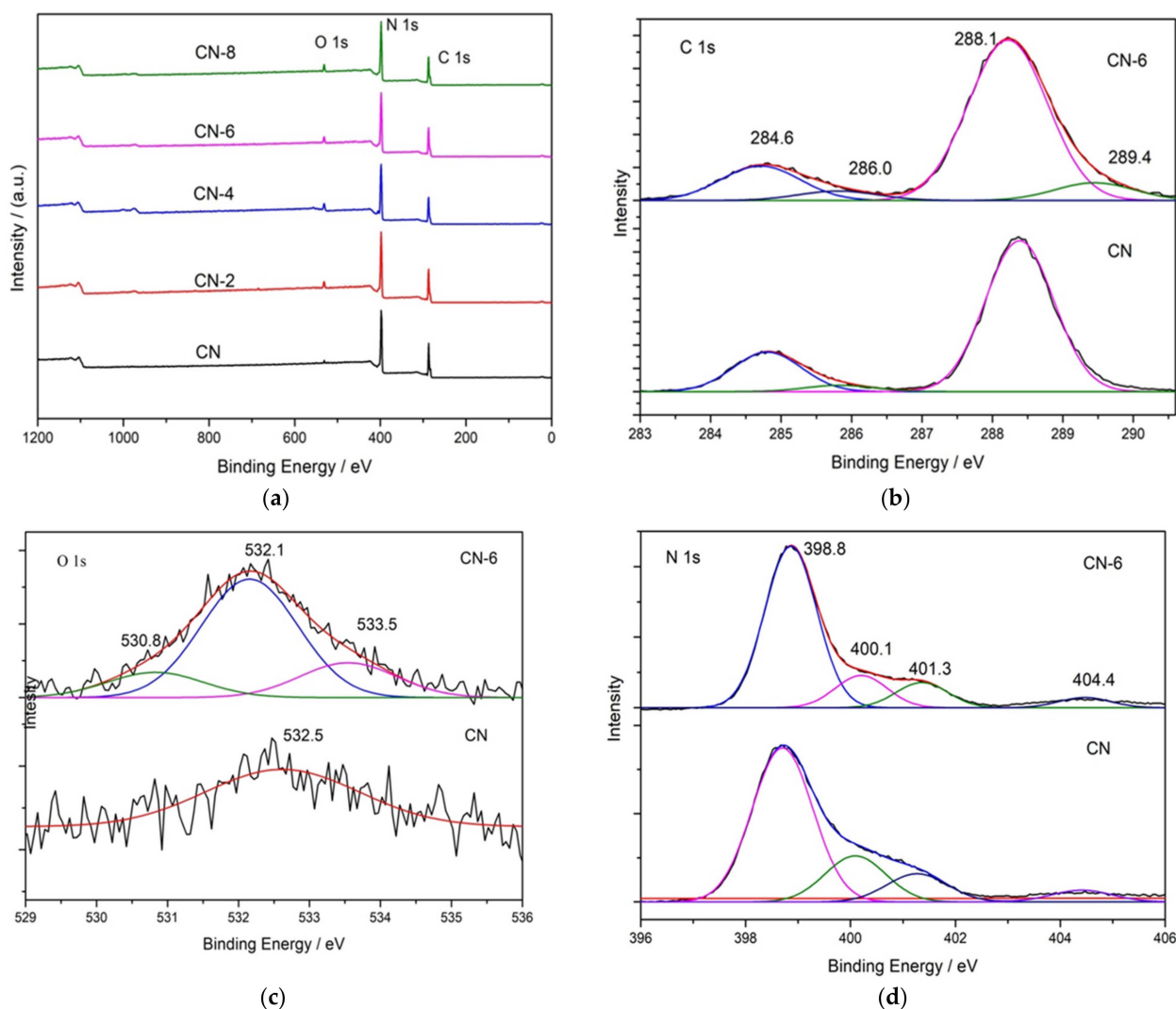


Figure 4. XPS survey of all samples (a) and high-resolution spectra in C 1s (b), O 1s (c), and N 1s (d); binding energy regions of CN and CN-6.

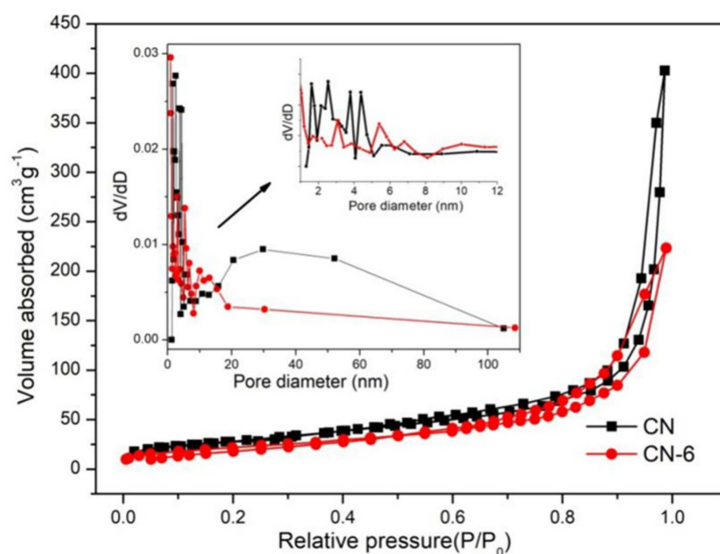


Figure 5. Adsorption–desorption isotherm of CN and CN-6.

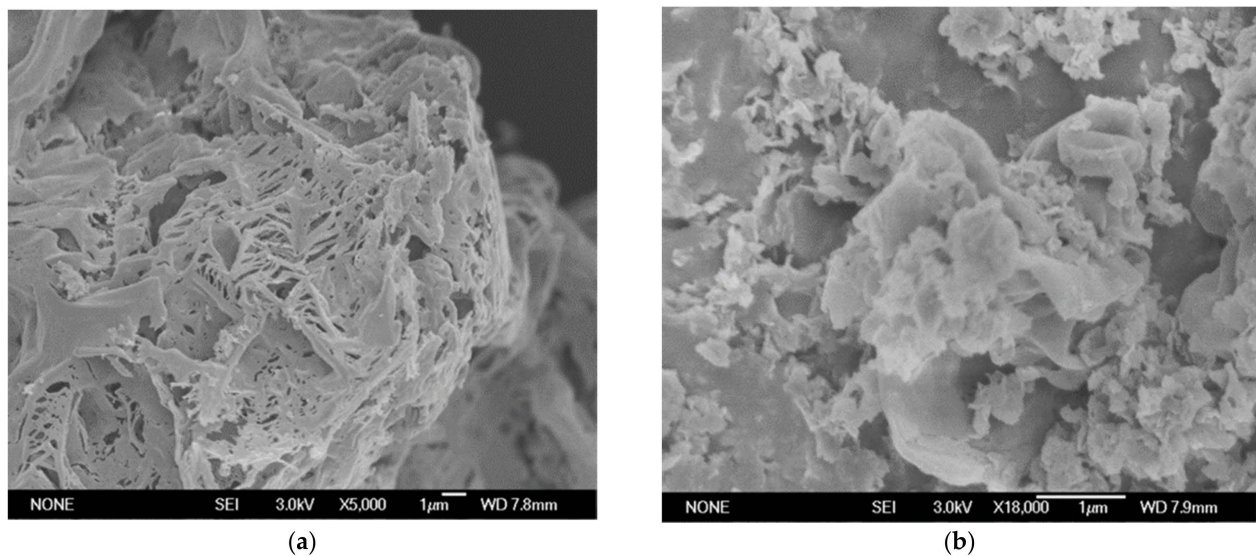


Figure 6. SEM images of (a) CN; (b) CN-6.

3.1.2. Optical Properties of the As-Prepared Photocatalysts

Diffuse reflectance UV-vis spectroscopy (DRS) was used to study the optical properties of the as-prepared samples. Figure 7a shows that a strong absorption band of bulk $g\text{-C}_3\text{N}_4$ was extended up to 450 nm, indicating an apparent absorption from ultraviolet to visible light. When CN-X was delaminated into nanosheets, its absorption edge had a slightly blue shift when compared to CN. CN-X, on the other hand, showed significant absorption in visible light, indicating that these samples can absorb visible light and be used for visible light photocatalysis. This absorption could be attributed to the presence of the oxygen element in the CN-X framework following acid-exfoliated CN [41]. The bandgaps (E_g) of CN and CN-X were also estimated using a plot of $(\alpha h\nu)^{1/2}$ vs. $h\nu$ ($n = 4$ for indirect transition). Figure 7b shows that the E_g value increased from 2.69 eV for CN to 2.87 eV for CN-6. This could be attributed to the ultrathin thickness's strong quantum confinement effect.

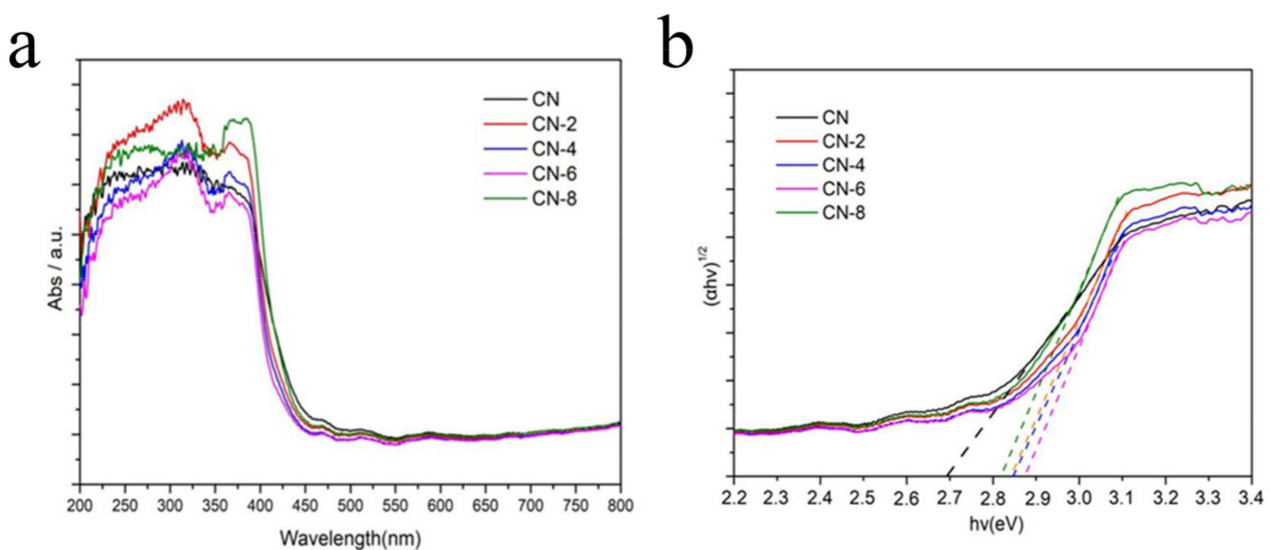


Figure 7. UV-vis/DRS of CN and CN-6 (a) and the corresponding band gap plots (b).

It is common practice to use photoluminescence (PL) spectra as an indirect measure of charge carrier separation effectiveness. Figure 8 shows the PL spectra of $g\text{-C}_3\text{N}_4$ and CN-6. In comparison to the bulk concentration of $g\text{-C}_3\text{N}_4$, CN-6 exhibited a somewhat blue

shift of the intrinsic PL peak, which corresponds to the UV-vis spectrum. Furthermore, the lower PL intensity of bulk g-C₃N₄ compared to CN-6, which may be due to surface defects of materials and stacking of nanosheets. It can be seen that a higher recombination rate is not the reason to improve the photocatalytic performance of the device in this paper [38].

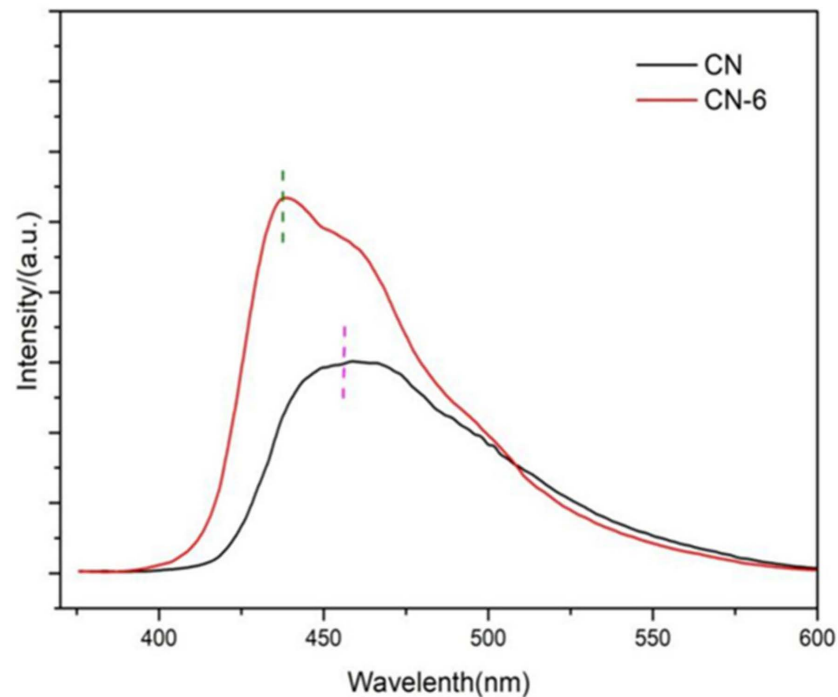


Figure 8. PL spectra of CN and CN-6.

3.2. Photocatalytic Activity and Stability

The photocatalytic performance of the as-prepared samples was assessed by the degradation of RhB and TC as a representative noxious pollutant under visible light irradiation conditions. The mixture of photocatalysts and impurities was magnetized and swirled in the dark for 30 min to create an adsorption–desorption equilibrium before being exposed to radiation. As shown in Figure 9a, the adsorption equilibrium was reached after 20 min of dark adsorption under these conditions, and we can obviously find that the adsorption capacity of CN-6 is stronger than that of CN. The large adsorption capability of the catalyst is advantageous to increase the photocatalytic performance because photocatalytic reactions take place on the catalyst surface. For comparison, a blank experiment without the photocatalyst was measured. The results in Figure 9a display that RhB can hardly decompose within 20 min of visible light irradiation, which can exclude the self-photolysis of RhB. The degradation performance values of CN, CN-2, CN-4, CN-6, and CN-8 were 89%, 80%, 78%, 99%, and 98%, respectively.

To gain insight into the photocatalytic activity of CN-X, the reaction kinetics of the degradation process were studied, and the result is shown in Figure 9b. The reaction kinetics were found to be appropriate for the pseudo-first-order model (Equation (1)), in which the slope of the fitted line can determine reaction rate constants (k).

$$-\ln(C/C_0) = kt \quad (1)$$

where C and C_0 are the concentrations of RhB at irradiation times t and 0 , and k is the apparent reaction rate constant. As a result, the pseudo-first-order-reaction kinetics (k) of RhB degradation relative to CN-6 was 0.16, which was twice as great as that of CN (0.08). The above result may be explained by the fact that the addition of functional groups containing oxygen causes the wells to disperse in the aqueous phase, which facilitates

the catalyst's interaction with the contaminants. In addition, the absorption edge of CN-6 exhibits a somewhat blue shift after nitric acid vapor treatment, resulting in the valence band position of CN-6 becoming positively shifted and the hole potential has stronger oxidizability. In addition, to test its universality, we also employed CN-X for the photodegradation of tetracycline hydrochloride. As shown in Figure 9c, the degradation of TC by CN-X system shows the same trend as that of RhB. According to the above experiments, the catalytic performance of $g\text{-C}_3\text{N}_4$ by nitric acid vapor treatment has been confirmed. The enhancement of photocatalytic activity of $g\text{-C}_3\text{N}_4$ mainly occurs because of nanosheet delaminated and the introduction of oxygen-containing groups caused by nitric acid vapor treatment. Reusability and stability are vital for photocatalysts in the practical applications. In order to investigate the reusability of CN-6, five successive cycles were performed for photodegrading RhB under the same conditions. As shown in Figure 9d, the degradation stays almost unchanged in the second recycle, and the degradation efficiency of RhB was still as high as 93% after five cycles, demonstrating that CN-6 possessed superior reusability.

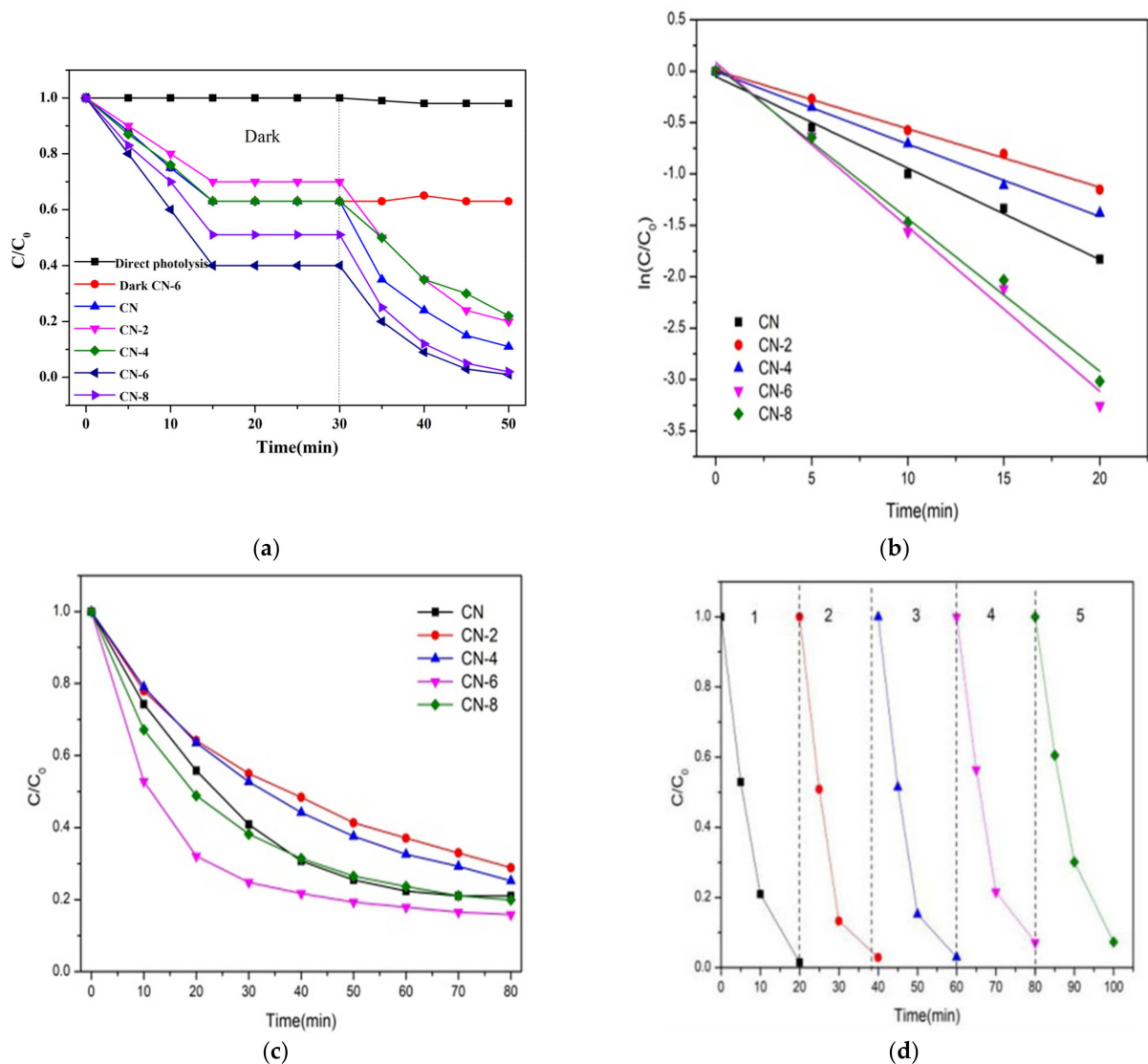


Figure 9. (a) Adsorption property and photocatalytic activity of samples towards the degradation of RhB under visible light irradiation; (b) the kinetic fit for RhB degradation; (c) photocatalytic activity of samples for TC breakdown under visible light and (d) during the photocatalytic breakdown of RhB over CN-6 when exposed to visible light, the photocatalytic activity cycles.

3.3. Discussion of Underlying Photocatalyst Mechanisms

Photoactive substances such as electrons, holes, superoxide radicals, and hydroxyl radicals are expected to photo-catalyze the degradation of RhB [42]. After using various quenchers to quench a variety of active species, we then aimed to determine the influence on the photocatalytic performance of CN-6, with the purpose of identifying the main active species in the photocatalytic process. Figure 10 shows that the degradation efficiency of RhB did not have an obvious decrease compared to the result without any scavenger after the addition of 10 mmol/L of isopropanol (IPA) as the OH quencher. This demonstrated that the predominant active species in the photocatalytic reaction were not the OH radicals. The fact that the degradation efficiency was unaffected by the addition of 10 mmol/L p-Benzoquinone (p-BQ) as an $\cdot\text{O}_2^-$ scavenger further demonstrated that O_2^- was not the main active species. This is due to the conduction band of CN-6 becoming more positive, resulting in the weaker reduction of electrons, which further affects the formation of O_2^- . In contrast, with the 10 mmol/L of triethanolamine (TEOA) in the form of h^+ scavenger, the degradation efficiency of RhB decreased by 69%. This demonstrated that h^+ was the major active species of the photocatalytic process.

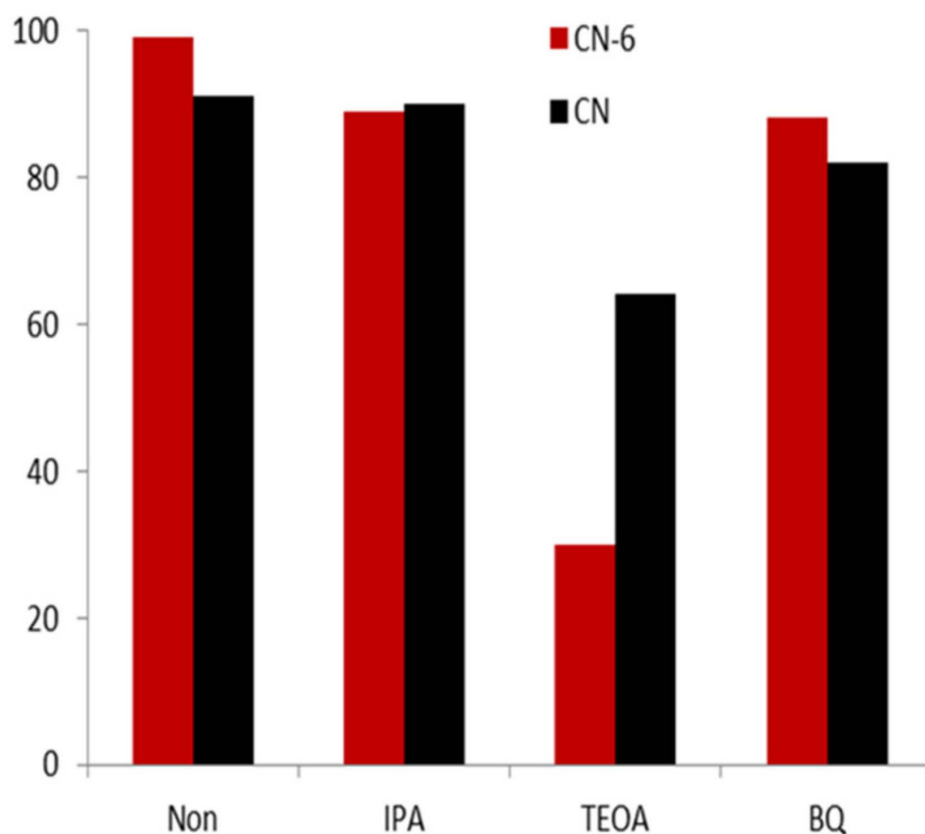


Figure 10. The trapping experiment of the active species during the photocatalytic degradation of RhB relative to CN-6 under visible light irradiation.

Based on the valence band minimum (VBM) roughly evaluated from the valence band X-ray photoelectron spectroscopy (Figure 11a) and E_g result from UV-vis absorption spectra, the conduction band minimum (CBM) could be roughly calculated according to the following equation: $E_g = \text{VBM} - \text{CBM}$

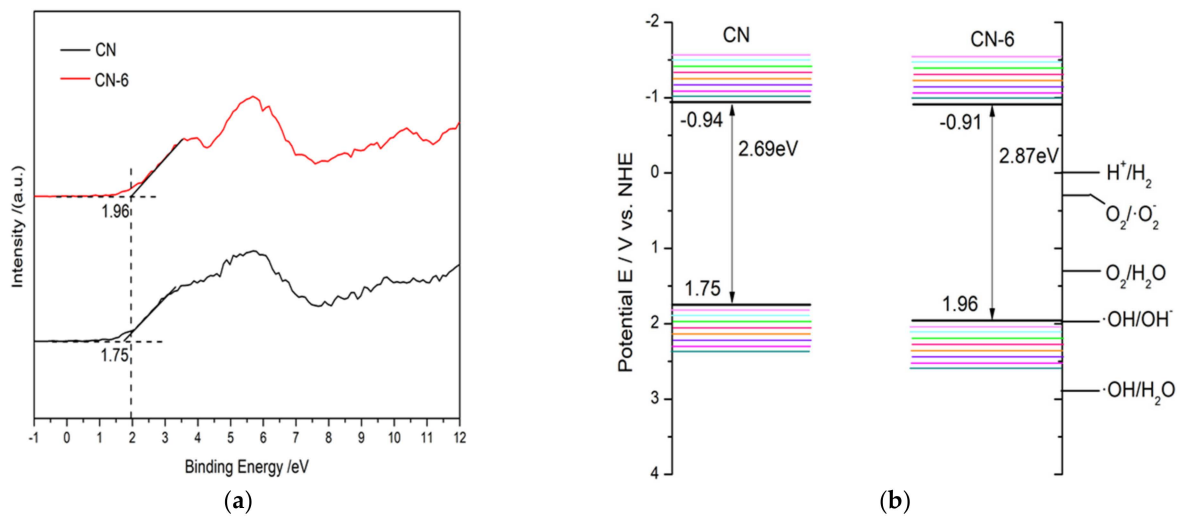


Figure 11. (a) The valence band X-ray photoelectron spectroscopy of CN and CN-6, and (b) band structures of CN and CN-6.

As a result, Figure 11b provides a schematic depiction of the band structures of the bulk forms of $g\text{-C}_3\text{N}_4$ and CN-6. The Eq. was expanded to 2.87 eV compared to the 2.69 eV of the bulk $g\text{-C}_3\text{N}_4$, which is attributed to the strong quantum confinement effect of the thickness of ultrathin. Correspondingly, the VBM of CN-6 was positively shifted to 1.96 eV from the 1.75 eV of bulk $g\text{-C}_3\text{N}_4$, indicating the oxidizability of the hole became stronger. Moreover, introducing oxygen-containing functional groups is said to promote visible light harvesting [28]. The process of RhB degradation over CN-6 is shown in Figure 12. In the presence of visible light irradiation, electrons on the VBM of CN-6 can be readily excited and transferred to the CBM of CN-6, thus leaving holes on the VBM. Photoinduced electrons will reduce O_2 adsorbed to the surface to generate O_2^- , which would be expected to oxidize RhB in an aqueous solution. The photoinduced holes will transfer to its surface and participate in the oxidation reaction [43]. More significantly, oxygen-containing functional groups such as C-OH and C=O can emerge and develop into electrophilic groups to prevent charge carriers from recombining.

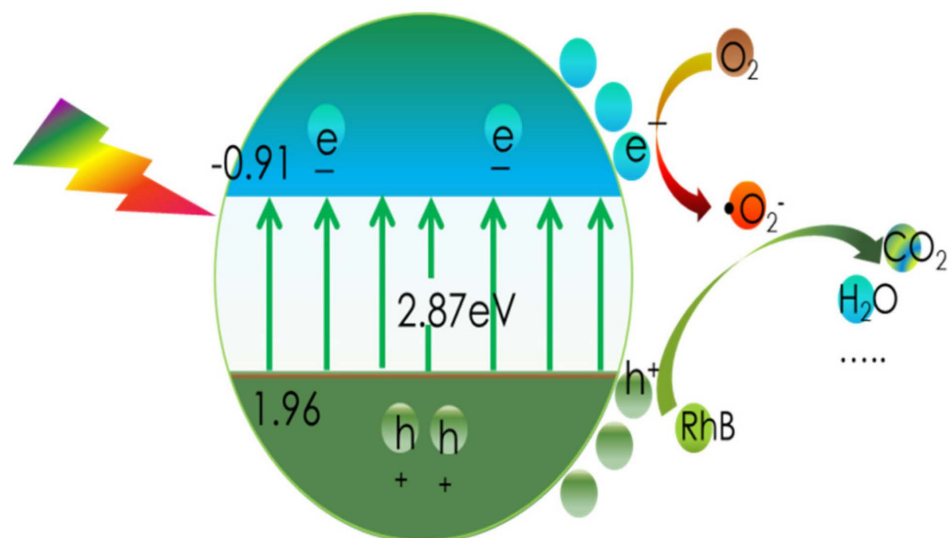


Figure 12. The process of RhB degradation over CN-6.

The high use of solar power, high surface area, and low recombination rate of photo-generated electron-hole pairs are widely recognized to be beneficial to the photo-activity

of a photocatalyst. However, the BET result shows that CN-6's surface area somewhat decreased, and the DRS result shows that CN-6's absorption edge exhibited a minor blue shift after being exposed to nitric acid vapor. The high photocatalytic activity of CN-6 could thus be caused by the effective dispersal into the aqueous phase and a stronger oxidation of the hole potential. The results clearly demonstrate that nitric acid vapor treatment promoted a blue shift, positively extended its valence band position, and enhanced the oxidizability of holes.

4. Conclusions

In brief, CN-X was synthesized successfully by treatment with urea-pyrolysis and nitric acid vapors. CN-6 possessed excellent photocatalytic performance and stability, which is ascribed to the blue shift and the abundance of oxygen containing functional groups on surfaces after nitric acid vapor treatment. On the one hand, the introduction of oxygen-containing functional groups in the process of lamellar exfoliation can make g-C₃N₄ disperse better in the aqueous phase, which facilitates the contact of the photocatalyst with pollutants. On the other hand, the absorption edge of CN-6 exhibits a somewhat blue shift, and the valence band position of the CN-6 is positively shifted after nitric acid vapor treatment, which leads to the stronger oxidation of hole potential. Furthermore, the results of the trap experiment demonstrated that photodegradation is dominated by h⁺. The results of this work provide a novel method for the self-modification of bulk g-C₃N₄, which can enhance the photoactivity of g-C₃N₄ for sustainable environmental restoration.

Author Contributions: Investigation, writing—original draft preparation, R.L.; writing—review and editing, B.W.; supervision, project administration, funding acquisition, R.W. All authors have read and agreed to the published version of the manuscript.

Funding: This research was funded by Shandong Provincial Independent Innovative Project for Important Key Technology Development (grant number 2014GJJS0501).

Institutional Review Board Statement: Not applicable.

Informed Consent Statement: Not applicable.

Data Availability Statement: Not applicable.

Conflicts of Interest: The authors declare no conflict of interest.

References

1. Singh, K.; Nowotny, J.; Thangadurai, V. Amphoteric oxide semiconductors for energy conversion devices: A tutorial review. *Chem. Soc. Rev.* **2013**, *42*, 1961–1972. [[CrossRef](#)] [[PubMed](#)]
2. Tong, H.; Ouyang, S.X.; Bi, Y.P.; Umezawa, N.; Oshikiri, M.; Ye, J.H. Nano-photocatalytic materials: Possibilities and challenges. *Adv. Mater.* **2012**, *24*, 229–251. [[CrossRef](#)]
3. Kudo, A.; Miseki, Y. Heterogeneous photocatalyst materials for water splitting. *Chem. Soc. Rev.* **2009**, *38*, 253–278. [[CrossRef](#)] [[PubMed](#)]
4. Zhang, J.; Chen, Y.; Wang, X. Two-dimensional covalent carbon nitride nanosheets: Synthesis, functionalization, and applications. *Energy Environ. Sci.* **2015**, *8*, 3092–3108. [[CrossRef](#)]
5. Reddy, P.A.K.; Reddy, P.V.L.; Kwon, E.; Kim, K.-H.; Akter, T.; Kalagara, S. Recent advances in photocatalytic treatment of pollutants in aqueous media. *Environ. Int.* **2016**, *91*, 94–103. [[CrossRef](#)] [[PubMed](#)]
6. Xiao, J.; Xie, Y.; Cao, H.; Wang, Y.; Zhao, Z. g-C₃N₄-triggered super synergy between photocatalysis and ozonation attributed to promoted OH generation. *Catal. Commun.* **2015**, *66*, 10–14. [[CrossRef](#)]
7. Weon, S.; Choi, W. TiO₂ nanotubes with open channels as deactivation-resistant photocatalyst for the degradation of volatile organic compounds. *Environ. Sci. Technol.* **2016**, *50*, 2556–2563. [[CrossRef](#)]
8. Fei, J.; Li, J. Controlled preparation of porous TiO₂-Ag nanostructures through supramolecular assembly for plasmon-enhanced photocatalysis. *Adv. Mater.* **2015**, *27*, 314–319. [[CrossRef](#)]
9. Pu, C.C.; Wan, J.; Liu, E.Z.; Yin, Y.C.; Li, J.; Ma, Y.N.; Fan, J.; Hu, X.Y. Two-dimensional porous architecture of protonated GCN and reduced graphene oxide via electrostatic self-assembly strategy for high photocatalytic hydrogen evolution under visible light. *Appl. Surf. Sci.* **2017**, *399*, 139–150. [[CrossRef](#)]
10. Zhu, B.; Zhang, J.; Jiang, C.; Cheng, B.; Yu, J. First principle investigation of halogen-doped monolayer g-C₃N₄ photocatalyst. *Appl. Catal. B Environ.* **2017**, *207*, 27–34. [[CrossRef](#)]

11. Wen, J.Q.; Xie, J.; Chen, X.B.; Li, X. A review on g-C₃N₄-based photocatalysts. *Appl. Surf. Sci.* **2017**, *391*, 72–123. [[CrossRef](#)]
12. Zheng, Y.; Zhang, Z.; Li, C.; Proulx, S. Surface hydroxylation of graphitic carbon nitride: Enhanced visible light photocatalytic activity. *Mater. Res. Bull.* **2016**, *84*, 46–56. [[CrossRef](#)]
13. Ong, W.J.; Tan, L.L.; Ng, Y.H.; Yong, S.T.; Chai, S.P. Graphitic carbon nitride (g-C₃N₄)-based photocatalysts for artificial photosynthesis and environmental remediation: Are we a step closer to achieving sustainability? *Chem. Rev.* **2016**, *116*, 7159–7329. [[CrossRef](#)]
14. Shi, L.; Chang, K.; Zhang, H.B.; Hai, X.; Yang, L.Q.; Wang, T.; Ye, J.H. Drastic enhancement of photocatalytic activities over phosphoric acid protonated porous g-C₃N₄ nanosheets under visible light. *Small* **2016**, *12*, 4431–4439. [[CrossRef](#)]
15. Yu, X.; Ng, S.F.; Putri, L.K.; Tan, L.L.; Mohamed, A.R.; Ong, W.J. Point-defect engineering: Leveraging imperfections in graphitic carbon nitride (g-C₃N₄) photocatalysts toward artificial photosynthesis. *Small* **2021**, *17*, 2006851. [[CrossRef](#)]
16. Hu, J.S.; Zhang, P.F.; An, W.J.; Liu, L.; Liang, Y.H.; Cui, W.Q. In-situ Fe-doped g-C₃N₄ heterogeneous catalyst via photocatalysis-Fenton reaction with enriched photocatalytic performance for removal of complex wastewater. *Appl. Catal. B Environ.* **2019**, *245*, 130–142. [[CrossRef](#)]
17. Jiang, L.B.; Yuan, X.Z.; Pan, Y.; Liang, J.; Zeng, G.M.; Wu, Z.B.; Wang, H. Doping of graphitic carbon nitride for photocatalysis: A review. *Appl. Catal. B Environ.* **2017**, *217*, 388–406. [[CrossRef](#)]
18. Guo, S.E.; Tang, Y.Q.; Xie, Y.; Tian, C.G.; Feng, Q.M.; Zhou, W.; Jiang, B.J. P-doped tubular g-C₃N₄ with surface carbon defects: Universal synthesis and enhanced visible-light photocatalytic hydrogen production. *Appl. Catal. B Environ.* **2017**, *218*, 664–671. [[CrossRef](#)]
19. Bao, Y.; Chen, K. Novel Z-scheme BiOBr/reduced graphene oxide/protonated g-C₃N₄ photocatalyst: Synthesis, characterization, visible light photocatalytic activity and mechanism. *Appl. Surf. Sci.* **2018**, *437*, 51–61. [[CrossRef](#)]
20. Tan, Y.; Shu, Z.; Zhou, J.; Li, T.; Wang, W.; Zhao, Z. One-step synthesis of nanostructured g-C₃N₄/TiO₂ composite for highly enhanced visible-light photocatalytic H₂ evolution. *Appl. Catal. B Environ.* **2018**, *230*, 260–268. [[CrossRef](#)]
21. Zhu, W.; Gao, X.; Li, Q.; Li, H.; Chao, Y.; Li, M.; Mahurin, S.M.; Li, H.; Zhu, H.; Dai, S. Controlled gas exfoliation of boron nitride into few-layered nanosheets. *Angew. Chem. Int. Ed.* **2016**, *55*, 10766–10770. [[CrossRef](#)] [[PubMed](#)]
22. Zhang, J.; Chen, X.; Takanabe, K.; Maeda, K.; Domen, K.; Epping, J.D.; Fu, X.; Antonietti, M.; Wang, X. Synthesis of a carbon nitride structure for visible-light catalysis by copolymerization. *Angew. Chem. Int. Ed.* **2010**, *49*, 441–444. [[CrossRef](#)] [[PubMed](#)]
23. Novoselov, K.S.; Geim, A.K.; Morozov, S.V.; Jiang, D.; Zhang, Y.; Dubonos, S.V.; Grigorieva, I.V.; Firsov, A.A. Electric field effect in atomically thin carbon films. *Science* **2004**, *306*, 666–669. [[CrossRef](#)] [[PubMed](#)]
24. Luo, J.; Chen, Q.; Dong, X. Prominently photocatalytic performance of restacked titanate nanosheets associated with H₂O₂ under visible light irradiation. *Powder Technol.* **2015**, *275*, 284–289. [[CrossRef](#)]
25. Chen, Q.; Luo, J.; Tao, Y.; Dong, X. Free-standing films of titanate nanosheets as efficient visible-light-driven photocatalysts for environmental application. *Mater. Lett.* **2015**, *145*, 111–114. [[CrossRef](#)]
26. Dong, X.; Cheng, F. Recent development in exfoliated two-dimensional g-C₃N₄ nanosheets for photocatalytic applications. *J. Mater. Chem. A* **2015**, *3*, 23642–23652. [[CrossRef](#)]
27. Niu, P.; Zhang, L.; Liu, G.; Cheng, H. Graphene-like carbon nitride nanosheets for improved photocatalytic activities. *Adv. Funct. Mater.* **2012**, *22*, 4763–4770. [[CrossRef](#)]
28. Yan, J.; Han, X.X.; Qian, J.J.; Liu, J.Y.; Dong, X.P.; Xi, F.N. Preparation of 2D graphitic carbon nitride nanosheets by a green exfoliation approach and the enhanced photocatalytic performance. *J. Mater. Sci.* **2017**, *52*, 13091–13102. [[CrossRef](#)]
29. Miao, H.; Zhang, G.W.; Hu, X.Y.; Mu, J.L.; Han, T.X.; Fan, J.; Zhu, C.; Song, L.; Bai, J.; Hou, X. A novel strategy to prepare 2D g-C₃N₄ nanosheets and their photoelectrochemical properties. *J. Alloys Compd.* **2017**, *690*, 669–676. [[CrossRef](#)]
30. Xu, J.; Zhang, L.; Shi, R.; Zhu, Y. Chemical exfoliation of graphitic carbon nitride for efficient heterogeneous photocatalysis. *J. Mater. Chem. A* **2013**, *1*, 14766–14772. [[CrossRef](#)]
31. Liu, J.; Zhang, T.; Wang, Z.; Dawson, G.; Chen, W. Simple pyrolysis of urea into graphitic carbon nitride with recyclable adsorption and photocatalytic activity. *J. Mater. Chem.* **2011**, *38*, 14398–14401. [[CrossRef](#)]
32. Kang, S.F.; Zhang, L.; Yin, C.C.; Li, Y.G.; Cui, L.F.; Wang, Y.G. Fast flash frozen synthesis of holey few-layer g-C₃N₄ with high enhancement of photocatalytic reactive oxygen species evolution under visible light irradiation. *Appl. Catal. B Environ.* **2017**, *211*, 266–274. [[CrossRef](#)]
33. Yang, Y.; Geng, L.; Guo, Y.; Meng, J.; Guo, Y. Easy dispersion and excellent visible-light photocatalytic activity of the ultrathin urea-derived g-C₃N₄ nanosheets. *Appl. Surf. Sci.* **2017**, *425*, 535–546. [[CrossRef](#)]
34. Zhang, Y.; Zhou, Z.; Shen, Y.; Zhou, Q.; Wang, J.; Liu, A.; Liu, S.; Zhang, Y. Reversible assembly of graphitic carbon nitride 3D network for highly selective dyes absorption and regeneration. *ACS Nano* **2016**, *10*, 9036–9043. [[CrossRef](#)]
35. Wang, F.L.; Chen, P.; Feng, Y.P.; Xie, Z.J.; Liu, Y.; Su, Y.H.; Zhang, Q.X.; Wang, Y.F.; Yao, K.; Lv, W.Y.; et al. Facile synthesis of N-doped carbon dots/g-C₃N₄ photocatalyst with enhanced visible-light photocatalytic activity for the degradation of indomethacin. *Appl. Catal. B Environ.* **2017**, *207*, 103–113. [[CrossRef](#)]
36. Wang, Y.; Wang, H.; Chen, F.; Cao, F.; Zhao, X.; Meng, S.; Cui, Y. Facile synthesis of oxygen doped carbon nitride hollow microsphere for photocatalysis. *Appl. Catal. B Environ.* **2017**, *206*, 417–425. [[CrossRef](#)]
37. Xiao, J.; Xie, Y.; Nawaz, F.; Jin, S.; Duan, F.; Li, M.; Cao, H. Super synergy between photocatalysis and ozonation using bulk g-C₃N₄ as catalyst: A potential sunlight/O₃/g-C₃N₄ method for efficient water decontamination. *Appl. Catal. B Environ.* **2016**, *181*, 420–428. [[CrossRef](#)]

38. Fan, C.; Feng, Q.; Xu, G.; Lv, J.; Zhang, Y.; Liu, J.; Qin, Y.; Wu, Y. Enhanced photocatalytic performances of ultrafine g-C₃N₄ nanosheets obtained by gaseous stripping with wet nitrogen. *Appl. Surf. Sci.* **2018**, *427*, 730–738. [[CrossRef](#)]
39. Li, H.J.; Sun, B.W.; Sui, L.; Qian, D.J.; Chen, M. Preparation of water-dispersible porous g-C₃N₄ with improved photocatalytic activity by chemical oxidation. *Phys. Chem. Chem. Phys.* **2015**, *17*, 3309–3315. [[CrossRef](#)]
40. Yang, X.; Qian, F.; Zou, G.; Li, M.; Lu, J.; Li, Y.; Bao, M. Facile fabrication of acidified g-C₃N₄/g-C₃N₄ hybrids with enhanced photocatalysis performance under visible light irradiation. *Appl. Catal. B Environ.* **2016**, *193*, 22–35. [[CrossRef](#)]
41. Cheng, F.; Wang, H.; Dong, X. The amphoteric properties of g-C₃N₄ nanosheets and fabrication of their relevant heterostructure photocatalysts by an electrostatic re-assembly route. *Chem. Commun.* **2015**, *51*, 7176–7179. [[CrossRef](#)] [[PubMed](#)]
42. Behera, A.; Kandi, D.; Majhi, S.M.; Martha, S.; Parida, K.M. Facile synthesis of ZnFe₂O₄ photocatalysts for decolourization of organic dyes under solar irradiation. *Beilstein J. Nanotechnol.* **2018**, *9*, 436–446. [[CrossRef](#)] [[PubMed](#)]
43. Meng, S.; Ye, X.; Ning, X.; Xie, M.; Fu, X.; Chen, S. Selective oxidation of aromatic alcohols to aromatic aldehydes by BN/metal sulfide with enhanced photocatalytic activity. *Appl. Catal. B: Environ.* **2016**, *182*, 356–368. [[CrossRef](#)]

Disclaimer/Publisher’s Note: The statements, opinions and data contained in all publications are solely those of the individual author(s) and contributor(s) and not of MDPI and/or the editor(s). MDPI and/or the editor(s) disclaim responsibility for any injury to people or property resulting from any ideas, methods, instructions or products referred to in the content.